RSC Advances

ROYAL SOCIETY OF CHEMISTRY

www.rsc.org/advances

Carbon dioxide capture by amino-functionalized ionic liquids: DFT based theoretical analysis substantiated by FT-IR investigation

Bobo Cao[1], Jiuyao Du[1], Shuangyue Liu[1], Xiao Zhu[1], Xuejun Sun[1], Haitao Sun[1*], Hui Fu[2*]*

[1]School of Chemistry and Chemical Engineering, Qufu Normal University, Qufu, Shandong, 273165, People's Republic of China

[2]College of Science, Chian University of Petroleum, Qingdao, Shandong, 266580, People's Republic of China

ABSTRCT

Carbon dioxide capture by amine-functionalized ionic liquids (IL), 1,2-dimethyl-(3-aminoethyl) imidazolium fluoride ([aEMMIM][F]), [aEMMIM][Cl], [aEMMIM][Br], [aEMMIM][I] were synthesized and characterized in both DFT simulation and experimental method. The most stable geometrical parameters of structures in this work were optimized at B3LYP/6-311++G(d,p) level by employing Gaussian09 program. The results showed that CO_2 can be chemically captured in ILs by forming carbamic acid with a 1:1 molar ratio stoichiometry. DFT simulation were performed to investigate the configuration variations of the reactants, intermediates, transition states and products, as well as energy barriers and vibration frequency changes in gas phase and using the conductor-like polarizable continuum model (CPCM) in aqueous solution. Vibration frequency obtained in DFT simulation was well consistent with experiment result via employing scaling factor. AIM and NBO analysis are also

carried out to investigate the nature and features of the studied structures at molecular level.

Keywords: carbon dioxide; ionic liquid; capture mechanism; haloid

1. Introduction

Although it is not a proven fact, there is a growing belief that global warming is occurring, and climate scientists hold the opinion that a major cause for this change is anthropogenic emission of greenhouse gases into the atmosphere. The post research have involved that carbon dioxide are the primary cause to the global warming.[1] Previous work indicates that global carbon dioxide energy related emissions are estimated to increase at the rate of 2.1% per year, which is consistent with the predicted consumption of fossil fuels for electricity generation.[2] Since renewable sources will not be sufficient to supply the required energy in the near future, fossil fuels may play an important role in electricity generation and supply.[3] Hence, capture of CO_2 from fossil fuel-derived flue gases has become an hot topic in both academic and industrial fields.[4]

Many methods have been developed on CO_2 capture, including membrane separation, adsorption, physical and chemical absorption.[5, 6] Ionic Liquid (IL) provides opportunities to develop novel technologies for CO_2 capture, since CO_2 can be dissolved in IL.[7, 8] *Brennecke et al.*[9, 10] reviewed the solubility of CO_2 in ILs, *Zhou et al.*[11] reported that the solubility of CO_2 in conventional ILs is limited. Nevertheless, various drawbacks are found in these methods, such as pollution, low efficiency and high cost. Recently, *Liang et al.*[12] presented a comprehensive review on the post-combustion carbon capture processes, in which many amine solvent-based CO_2 capture plants were provided with an in-depth understanding of the chemical

absorption of CO_2 using amine-based reactive solvents. *Chau et al.*[13] reported that CO_2 absorption efficiency increased considerably when the amine was added to conventional ILs and then increased several-fold when moisture was present in the amine–ILs solution, compared to conventional ILs. In order to promote the efficiency of CO_2 absorption in ILs, *Bates and Sánchez*[14, 15] and their co-workers designed amine-functionalized ILs by combining the advantages of the alkanolamine solution and ILs, which was supposed to absorb CO_2 chemically. Previous computational studies of *Gonzalez-Miquel et al.*[16] reported the impact of the functionalization of the ionic liquids with amines for chemical absorption of CO_2. In 2014, *Gonzalez-Miquel et al.*[17] further studied the behavior of CO_2 capture in the mixtures of ILs and molecular amines to provide further understanding of the behavior of these systems via experimental and computational analysis. Carbonic anhydrase mimics, containing the salen-like ligand bis(hydroxyphenyl)phenanthroline, have been used to enhance CO_2 absorption in amine-based capture solvent.[18] *Gurkan and Xue*[4, 19] pointed out that higher CO_2 absorption capacity with the 1:1 (CO_2: IL) mole ratio could be accomplished by tethering an amine on both the anion and cation of ILs. The amine-functionalized IL has been chosen as the most promising candidate for CO_2 capture. Since amine-functionalized IL has been employed in CO_2 capture by *Sun et al.*[20], many features on the capture progress are ambiguous.

In this work, four imidazolium-based ILs, 1,2-dimethyl-(3-aminoethyl) imidazolium fluoride ([aEMMIM][F]), [aEMMIM][Cl], [aEMMIM][Br], [aEMMIM][I] are synthesized and investigated systematically by both theoretical and experimental methods. The reactants (R), intermediates (IM), transition states (TS) and products (P) have been obtained and characterized by the method of Fourier transform infrared (FT-IR ATR) spectra of 2BP8HQ and density function theory

(DFT). The correctness of TS structure has been testified by intrinsic reaction coordinate (IRC) calculation. The vibrational frequency in experiment is well consistent with the result in DFT simulation. The bond nature and proton transfer process are analyzed by the vibrational frequencies analyses (VFA), theory of nature bond orbital (NBO) and atoms in molecules (AIM).

2. Experimental methods and material

CO_2 is supplied by Jinan Deyang Special Gas Co., Ltd with a purity of 99.99%. 1,2-Dimethylimidazolium is obtained from Xiya Reagent. Hydrofluoric acid is supplied by Shenyang Shenbei Wan Xiang Chemical Co., LTD. Hydrochloric acid, Hydrogen bromide and hydrogen iodide are supplied by Beijing Analytical Instrument Factory. 2-Bromothylamine hydrobromide is supplied by Shanghai Nanxiang Reagent Co., Ltd.

[aEMMIM][F], [aEMMIM][Cl], [aEMMIM][Br], [aEMMIM][I] are synthesized with a purity of 99%. The water contents in the ILs are all less than 800 ppm, as measured by Karl Fisher titration. [aEMMIM][Br] is taken as an example to mainly discuss the CO_2 capture progress. Physical properties of [aEMMIM][Br], including density (1.215-1.360 g/cm^3) and viscosity (396.3-428.5 mPa·s), are also measured at melting point (50 ℃). After the reaction of 1,2-dimethyl imidazolium with 2-bromoethylamine hydrobromide, we assemble the cation in ethanol. The product, [aEMMIM][Br], is obtained via the ion exchange with hydrochloric acid after the solvent and solid residue have been removed. Fourier-transform mass spectrometry (FT-MS) has verified the structure and composition of the as-synthesized IL. Finally, the product is dried under vacuum at 90℃ for 72h.

In order to get more data, an attenuated total reflection Fourier transform infrared

(FT-IR ATR) spectra of 2BP8HQ is registered using Varian FTS1000 FT-IR spectrometer with Diamond/ZnSe prism (4000–525 cm^{-1}; number of cans: 250; resolution: 1 cm^{-1}) was used to measure the infrared spectra of [aEMMIM][Br].

3. Computational methods

The geometries of the R, IMs, TS and P are firstly optimized at B3LYP/6-31G level[21] and also characterized as global minima by frequency analyses. Then, geometry optimizations are performed at B3LYP/6-311++G(d,p) level, in which pseudopotential is employed to describe the inner core orbitals iodine. Previous computational studies of *Palomar et al.*[22] and *Sun et al.*[20] have confirmed the suitability of the computational level to study the behaviour of ionic liquids for CO_2 capture. Frequency calculations are carried out to verify the validity of the optimized structures. The values of frequency are computed at the same level containing certain systematic errors.[23] At the same time, measures are taken to account for errors due to the neglecting electron correlation and the basis set incompleteness. B3LYP systematic errors are considered with scaling factor of 0.983 for below 1700 $cm^{-1}$and 0.958 for above 1700 cm^{-1}, which is employed by many people.[23-25] IRC are used to verify the energy profiles connecting the TS structure to the two desired global minima of the proposed mechanism scheme. The counterpoise (CP) method is used to estimate the interaction energy (ΔE) including the basis set superposition errors (BSSE) correction. AIM and NBO analyses are performed to study the nature and characteristic of bonds at B3LYP/6-311++G(d,p) level. Subsequently, the solvent water for above ILs had been taken into account by the conductor-like polarizable continuum model (CPCM) with united-atom Kohn–Sham (UAKS) radii.[26] The DFT calculations are carried out with Gaussian09 package.[27]

4. Results and discussion

4.1. Electrostatic potential analysis

The electrostatic potential (ESP) of [aEMMIM][F], [aEMMIM][Cl], [aEMMIM][Br] and [aEMMIM][I] are shown in Figure 1, respectively. It can be easily found that the electrostatic potential surface at sites close to the polar group is influenced by the stereo structure and the charge density distribution. It indicates that the highly negative regions (red) of $[Br]^-$ anion are found away from $[aEMMIM]^+$ and show high activity on the electronegative Br atom. In contrast, the highly positive regions (blue) in $[aEMMIM]^+$ are localized on the hydrogen atom of the alkyl groups, which can be considered as possible sites for nucleoplilic attack of C26 atom in CO_2 molecular. It is reliable that C26 atom in CO_2 attacks the N22 atom in $[aEMMIM]^+$ according to ESP analysis, and the assumption is coincide with the following analysis.

4.2. Geometry and energy analysis

[aEMMIM][Br] is taken as an example to mainly discuss the capture mechanism of CO_2 in ILs. [aEMMIM][Br] and CO_2 has been fully optimized at B3LYP/6-311++G(d,p) level, the geometrical parameters involving various species of [aEMMIM][Br] and CO_2 are shown in Figure 2. For the other three ILs, the geometrical parameters are given in Figure S1 (Electronic Supporting Information). The most stable conformers of [aEMMIM][Br] and CO_2 are obtained and the energy are -3013.487562 and -188.635227 a.u., respectively. According to the IRC calculation, two desired global minima states in the process are obtained, which indicate this species is the real TS, and imaginary frequency (-1739.73 cm^{-1}) has future confirmed this result. The potential energy surface (PES) profile of

[aEMMIM][Br] and CO_2 is depicted in Figure 3. The PES profiles of the other three ILs are given in Figure S2. Firstly, when CO_2 approaches to [aEMMIM][Br], O28 atom in CO_2 molecule forms hydrogen bond with H23 in $[aEMMIM]^+$ and the bond distance is 3.51068 Å. For TS, the proton H23 on amino-group of $[aEMMIM]^+$ transfers to O28 atom of CO_2 and the bond distances of N22-H23 and newly-formed O28-H23 are 1.0145 Å (R) and 0.9661 Å (P), respectively. It is mentionable that the bond distance between N22 and C26 is shorten from 2.9193 (IM) via 1.5478 (TS) to 1.3691 Å (P), which suggests that the N22-C26 bond is newly formed. It can be easily found that the C26-O28 bond distance gradually extends from 1.1601 (IM) via 1.2898 (TS) to 1.3588 Å (P). Simultaneously, the C26-O27 bond distance gradually extends from 1.1630 (IM) via 1.1965 (TS) to 1.2129 Å (P). The tetra-atomic ring is distinctly observed containing N22, H23, O28 and C26 atoms, which is consistent with the following analysis.

The energy barrier analysis is carried out based on the difference of the zero-point energy of R, TS and P, in which the conductor-like polarizable continuum model (CPCM) is employed to approximately estimate the solvent effect. The black line in Figure 3 describes the energy diagram in the gas phase, and the red line corresponds to the energy diagram in the water solution. It can be seen from Figure 3, the energy barrier is estimated as high as 169.43kJ/mol between IM and TS in gas phase, and this step can be considered as rate-determining step. Meanwhile, the energy barrier decreases to 152.61kJ/mol in water solution is found. The result suggests that it is easier to get the P in water solution. Simultaneously, the energy of P is found higher than IM by 11.47 kJ/mol in the gas phase and 108.12 kJ/mol in water solution, respectively, which indicates that IM is more stable than P and the reaction is an endothermic absorption. The results above indicate CO_2 capture process in water

174 solution is kinetically and thermodynamically more favorable than that in the gas
175 phase. In this process, water molecule may assist the proton transfer from amine
176 group to CO_2 and decrease the steric effect in this process.
177
178 **4.3. Vibration frequency analysis**
179 Main vibration frequency variations of CO_2, [aEMMIM][Br] and
180 [aEMMIM][Br]+CO_2 calculated at B3LYP/6-311++G(d,p) level are listed in Table 1.
181 Vibrational frequencies of [aEMMIM][Br] and [aEMMIM][Br]+CO_2 are determined
182 by (FTIR) spectrometer. Table S1 and Table S2 show the wave numbers of the bands,
183 which are calculated at B3LYP/6-311++G(d,p) level. The theoretical and
184 experimental IR spectrum comparisons between [aEMMIM][Br] and
185 [aEMMIM][Br]+CO_2 are depicted in Figure 4, respectively. As no imaginary
186 frequency is found in IM and P and only one imaginary frequency is found in TS (-
187 1739.73 cm^{-1}), the results based on these structures are reliable.
188 The scaling factors are also employed to scale down the calculated wave numbers
189 obtained with B3LYP method so as to improve the agreement with the experiments
190 result (0.983 for below 1700 cm^{-1} and 0.958 for above 1700 cm^{-1}).[23-25] The gap
191 between the experimental and computational frequencies can be attributed to the fact
192 that the theoretical result is obtained from a single molecule in gas phase, which is
193 contrary to the experimental result recorded in the presence of intermolecular
194 interactions. It is reasonable to believe that the experimental result of vibration
195 frequency is limited by experimental conditions, however, the computational result
196 can be considered as a guide to explore the real vibrational modes. This means our
197 vibration frequency analysis, combining theoretical and experimental results, is
198 reliable.

Comparing the results in Table 1, one can easily find that the value of the vibrational frequency of CO_2 group in IM and TS is smaller than pure carbon dioxide molecule. For IL, IM, TS and P, obvious changes are observed in vibration frequency and vibration mode on some groups in the reaction. The rupture of N22-H23 bond and the formation of O28-H23 bond have been well confirmed by the disappearance of symmetric stretching vibration $\nu_s(\text{-}NH_2)$ in 3418.29 cm^{-1} and asymmetric stretching vibration $\nu_{as}(\text{-}NH_2)$ in 3544.87 cm^{-1} in IM and the presence of stretching vibration ν(-OH) in 3634.93 cm^{-1} in P, which is consistent with geometry analysis and following AIM analysis. The experimental results are better agreement with the scaled calculated values. In Figure 4, we also find the disappearance of $\nu_{as}(\text{-}NH_2)$ and a red-shift of ν_s(-NH) in the product. Meanwhile, the C26-H23 bond is extended gradually from 1.0145 (IL) via 1.0154 (IM) to 1.2911 (TS) Å and then break down. Simultaneously, the IR intensity of $\nu_s(\text{-}NH_2)$ in IL is found higher than that in IM. The symmetric stretching vibration $\nu_s(\text{-}CO_2)$ of IM and the symmetric stretching vibration $\nu_s(\text{-}CO_2)$ of TS have a red-shift from 1368.18 to 1272.69 cm^{-1}, which can be interpreted that H23 proton of $\text{-}NH_2$ transfer to O27 atom of CO_2 and the C=O double bond stretched to C-O single bond. It is well consistent with the emergences of the symmetric vibration ν(-C26=O27) and ν(-C26-O28) of P (Figure 4). Besides, the emergences of rocking vibration ρ(-OH) in 1198.572 cm^{-1}, bending vibration δ(-O28-H23) in 1318.498 cm^{-1}, the stretching vibration ν(-O28-H23) in 3634.93 cm^{-1} for P gives a further demonstration on the proton transfer process. The peaks emerge in Figure 4 are also subject to the results above. Bending vibration $\delta(\text{-}NH_2)$ at 1659.76 cm^{-1}, symmetric stretching vibration $\nu_s(\text{-}NH_2)$ at 3418.29 cm^{-1}, asymmetric stretching vibration $\nu_{as}(\text{-}NH_2)$ at 3544.87 cm^{-1} and asymmetric stretching vibration $\nu_{as}(\text{-}CO_2)$ in 3412.17 cm^{-1} disappear from IM to P. The bending vibration δ(-OH) at 1318.498 cm^{-1},

bending vibration δ(-NH) at 1524.653 $cm^{-1}$and rocking vibration ρ(-OH) at 1198.572 cm^{-1} are found, which further confirm the fact that a carbonic acid species is produced due to the interaction between the amino group and CO_2. The presence of peak around 3600 cm^{-1} in Figure 4 corresponds to carbonyl group, which is well consistent with the appearance of the new peak at 3634.93 cm^{-1} corresponding to ν(-OH) of -COOH in Table 1. The stretching vibration ν(-OH) is also observed in Figure 4, coinciding with the O-H (0.9661 Å) bond distance in –COOH.[28]

4.4. AIM analysis

The electron density (ρ(r)) and the Laplacian of the electron density ($\nabla^2\rho(r)$) as well as the eigenvalue (λ_i) of Hessian matrix among the IM, TS, and P calculated at B3LYP/6-311++G(d,p) level are shown in Table 2. For [aEMMIM][Cl], the values are shown in Table S3. Molecular graph of [aEMMIM][Br]+CO_2, depicted using WFN file produced in Gaussian09 program at B3LYP/6-311++G(d,p) level, are shown in Figure 6. Among Figure 6, the red point and yellow point represent the bond critical point (BCP) and ring critical point (RCP), respectively.

Since ρ(r) is related to the bond strength, the ρ(r) of N22-H23 bond is 0.33104 a.u. in IM and it is much larger than that 0.15688 a.u. in TS, which indicates that N22-H23 bond strength become weaker, from IM to TS. Besides, the ε of N22-H23 increase from 0.04282 to 0.1114 also indicates the rupture trend of N22-H23 bond. For N22-C26 bond, $\nabla^2\rho(r)$ decrease from 0.03741 (IM) via -0.4328 (TS) to -0.9836 a.u. (P), which indicates a weak electrostatic interaction between amino-group and CO_2 in IM has become to a covalent interaction in P and the covalent bond of N22-C26 is newly formed. Interestingly, the ρ(r) value of N22-C26 bond in P (0.32289 a.u.) is larger than that in TS (0.22592 a.u.), which is consistent with the larger $\nabla^2\rho(r)$

value in P. Both of $\rho(r)$ and $\nabla^2\rho(r)$ value have confirmed the process of the strong covalent bond of N22-C26. As the C26-O28 double bond becomes to a weaker single bond from IM to P, the $\rho(r)$ value decrease from 0.45552 (IM) via 0.35641 (TS) to 0.29651 a.u. (P), coinciding with the geometry analysis. Simultaneously, the larger $\rho(r)$ (0.36243 a.u) and $\nabla^2\rho(r)$ (-2.520 a.u.) value of O28-H23 in P indicate the formation of the strong O-H covalent bond. And this is well consistent with the O28-H23 bond distance decrease from 1.2898 (TS) and 0.9661 Å (P). A tetra-atomic ring formed by N22, H23, O28 and C26 atoms can be observed in Figure 5, which can be confirmed by RCP in the ring center.

4.5. NBO analysis

NBO theories are carried out to obtain the intrinsic property of these interactions among IM, TS and P. Taking [aEMMIM][Br] as an example, the donor-acceptor interactions and their second order perturbation stabilization energies, E(2), as well as the energy gap (difference between the highest occupied orbital and the lowest unoccupied orbital) calculated at the B3LYP/6-311++G(d,p) level are given in Table 3. For [aEMMIM][Cl] and [aEMMIM][F], the values are shown in Table S4 and Table S5, respectively. The schematic graphs of electron transfer of Br system based on the NBO analysis are shown in Figure 6.

In Table 3, the lone pair electrons of O28 atom transfer to the region around C26-O27 bond in three different types in IM, with LP(3)O28→BD*(2)C26-O27 possessing the largest E(2) (509.4 kJ/mol) and large areas of orbital overlap (Figure 6a). These large E(2) indicate the presence of strong orbital interactions and the C26-O28 bond is becoming weaker due to the lack of electrons around O28 and strong orbital interactions, coinciding with geometry and AIM analysis. The same analysis

also suitable for LP(1)N22→BD*(1)C26-C19 and it can interpret the rupture of N22-H23 bond. Then, the large E(2) (505.6 kJ/mol) and small energy gap (0.49 a.u.) as well as large areas of orbital overlap (Figure 6b) suggest the existence of strong interaction between electron donor (LP(2)O28) and acceptor (BD*(1)N22-H23) in TS. Simultaneously, the lone pair electron transfer from LP(2)O27 to BD*(1)N22-C26 is also found and this can promote the formation of N22-C26 bond in P. Comparing with LP(3)O28→BD*(2) C26-O27 in TS, the decrease of E(2) from 240.2 to 129.3 kJ/mol and the increase of energy gap from 0.35 to 0.60 a.u. of LP(2)O28→BD*(1)C26-O27 (Figure 6c) can be attributed to weaker orbital interaction. The lone pair electron of LP(1)N22 transfer to BD*(1)C26-O28 leading to the break of N22-H23 bond and the formation of C26-O28 covalent bond. The BD*(1)(C26-N22) as an acceptor of lone pair electron from LP(1)O28 with E(2) of 90.79 kJ/mol, the electron density in BCP (ρ(r) in AIM analysis) between C26 and N22 atoms increases from 0.22592 a.u. (TS) to 0.32289 a.u. (P) in contrary of the ρ(r) decrease of O28-C26 from 0.35641 a.u. (TS) to 0.29651 a.u. (P). These results are well consistent with the other analysis method in this paper.

5. Conclusions

Amine-functionalized ionic liquids (ILs) [aEMMIM][F], [aEMMIM][Cl], [aEMMIM][Br] and [aEMMIM][I] are designed and synthesized and they all show excellent CO_2 capture capacity with a 1:1 molar ratio. Both DFT simulation and experimental results indicate CO_2 can be efficiently and tightly captured by amine-functional ILs, and the process should be considered as chemically absorption due to the presence of carbamic acid. DFT calculation is employed to further uncover the mechanism between CO_2 and Amine-functionalized ILs. The small difference

between the observed and scaled parameters of vibration frequency suggests this result is feasible. The geometries of R, IM, TS and P are fully optimized at B3LY/6-311++G(d,p) level, and harmonic vibrational frequency is used to confirm their real configuration. Comparing with gas phase, the small energy barrier in water solution indicates the reaction is easy going in aqueous solution. The amino-functionalized ILs captured CO_2 by forming carbamic acid. Simultaneously, AIM and NBO analyses are also carried out to investigate the nature and features of the studied structures at molecular level.

Table and Figure captions

Table 1 Main vibration frequency of CO_2, -NH_2, IM, TS and P for Br system optimized at B3LYP/6-311++G(d,p) levels.

Table 2 The electron density (ρBCP), Laplacian of the electron density (∇^2ρBCP) and matrix eigenvalues (λ_1, λ_2, λ_3) for Br system at B3LYP/6-311++G(d,p) level.

Table 3 The main donor-acceptor interactions and their second order perturbation stabilization energies, E(2) as well as orbital energy gap for Br system calculated at B3LYP/6-311++G(d,p) level.

Figure 1 3D plots of the electrostatic potential surface for the pure ILs, including [aEMMIM][F], [aEMMIM][Cl], [aEMMIM][Br], [aEMMIM][I], optimized at B3LYP/6-311++G(d, p) level, respectively.

Figure 2 Geometrical parameters of Br system, including [aEMMIM][Br], IM, TS and P, optimized at B3LYP/6-311++G(d, p) level, respectively. (in Å)

Figure 3 Potential energy surface (PES) profile of [aEMMIM][Br] capture CO_2 optimized at B3LYP/6-311++G (d, p) level.

Figure 4 Computational IR spectrum (a) and experimental IR spectrum (b) of [aEMMIM][Br] and [aEMMIM][Br]+CO_2.

Figure 5 Molecular graph of [aEMMIM][Br] capture CO_2 optimized at B3LYP/6-311++G(d,p) level, red points and yellow points correspond to bond critical point(BCP) and ring critical point(RCP), respectively.

Figure 6 The schematic graphs of electron transfer of Br system based on the NBO analysis (a form IM, b for TS and C for P).

ASSOCIATED CONTENT

Supporting Information

This material is available via the Internet at the website of RSC Advance for free.

We are gonging to a color printing when this manuscript being accepted by RSC Advance.

AUTHOR INFORMATION

Corresponding Author

*E-mail:sunhaitao1960@126.com; sxjsunxuejun@163.com; fuhui@upc.edu.cn

Tel.: +86-0537-4456765

Other Authors

E-mail: qufucaobobo@163.com; jwyhbxr@163.com; liushuangyue0919@163.com; qfnu_zx@163.com

Acknowledgements

This work was supported by the National Natural Science Foundation of China (No. 21206085 and 21203250).

References

1. J. Gibbins and H. Chalmers, *Energy Policy*, 2008, 36, 4317-4322.
2. N. Lior, *Energy*, 2008, 33, 842-857.
3. N. MacDowell, N. Florin, A. Buchard, J. Hallett, A. Galindo, G. Jackson, C. S. Adjiman, C. K. Williams, N. Shah and P. Fennell, *Energy Environ. Sci.*, 2010, 3, 1645-1669.
4. Z. Xue, Z. Zhang, J. Han, Y. Chen and T. Mu, *Int. J. Greenhouse Gas Control*, 2011, 5, 628-633.
5. J. E. Bara, R. D. Noble and D. L. Gin, *Ind. Eng. Chem. Res.*, 2009, 48, 4607-4610.
6. Q. Wang, J. Luo, Z. Zhong and A. Borgna, *Energy Environ. Sci.*, 2011, 4, 42-55.
7. Á. Pérez-Salado Kamps, D. Tuma, J. Xia and G. Maurer, *J. Chem. Eng. Data*, 2003, 48, 746-749.
8. A. H. Jalili, A. Mehdizadeh, M. Shokouhi, H. Sakhaeinia and V. Taghikhani, *J. Chem. Thermodyn.*, 2010, 42, 787-791.
9. J. L. Anderson, J. K. Dixon and J. F. Brennecke, *Accounts Chem. Res.*, 2007, 40, 1208-1216.
10. K. A. Baumert, T. Herzog and J. Pershing, *Navigating the numbers: Greenhouse gas data and international climate policy*, World Resources Inst, 2005.
11. L. Zhou, J. Fan, X. Shang and J. Wang, *J. Chem. Thermodyn.*, 2013, 59, 28-34.
12. Z. H. Liang, W. Rongwong, H. Liu, K. Fu, H. Gao, F. Cao, R. Zhang, T. Sema, A. Henni and K. Sumon, *Int. J. Greenhouse Gas Control*, 2015, 40, 26-54.
13. J. Chau, G. Obuskovic, X. Jie, T. Mulukutla and K. K. Sirkar, *Ind. Eng. Chem. Res.*, 2013, 52, 10484-10494.
14. E. D. Bates, R. D. Mayton, I. Ntai and J. H. Davis, *J. Am. Chem. Soc.*, 2002, 124, 926-927.
15. L. Galán Sánchez, G. Meindersma and A. De Haan, *Chem. Eng. J.*, 2011, 166, 1104-1115.
16. M. Gonzalez-Miquel, M. Talreja, A. L. Ethier, K. Flack, J. R. Switzer, E. J. Biddinger, P. Pollet, J. Palomar, F. Rodriguez and C. A. Eckert, *Ind. Eng. Chem. Res.*, 2012, 51, 16066-16073.
17. M. Gonzalez-Miquel, M. Massel, A. DeSilva, J. Palomar, F. Rodriguez and J. F. Brennecke, *J. Phys.Chem. B*, 2014, 118, 11512-11522.
18. R. A. Kelsey, D. A. Miller, S. R. Parkin, K. Liu, J. E. Remias, Y. Yang, F. C. Lightstone, K. Liu, C. A. Lippert and S. A. Odom, *Dalton T.*, 2016, 45, 324-333.
19. B. E. Gurkan, J. C. de la Fuente, E. M. Mindrup, L. E. Ficke, B. F. Goodrich, E. A. Price, W. F. Schneider and J. F. Brennecke, *J. Am. Chem. Soc.*, 2010, 132, 2116-2117.
20. H. Sun, X.-q. Zhou, Z. Xue, Z.-y. Zhou and T. Mu, *Int. J. Greenhouse Gas Control*, 2014, 20, 43-48.
21. A. D. Becke, *J. Chem. Phys.*, 1993, 98, 5648-5652.
22. J. Palomar, M. Gonzalez-Miquel, A. Polo and F. Rodriguez, *Ind. Eng. Chem. Res.*, 2011, 50, 3452-3463.
23. N. Sundaraganesan, S. Ilakiamani, H. Saleem, P. M. Wojciechowski and D. Michalska, *Spectrochim. Acta A*, 2005, 61, 2995-3001.
24. J. P. Merrick, D. Moran and L. Radom, *J. Phys.Chem. A*, 2007, 111, 11683-11700.
25. M. Karabacak, M. Çınar, A. Çoruh and M. Kurt, *J. Mol. Struct.*, 2009, 919, 26-33.
26. V. Barone, M. Cossi and J. Tomasi, *J. Comput. Chem.*, 1998, 19, 404-417.
27. M. Frisch, G. Trucks, H. B. Schlegel, G. Scuseria, M. Robb, J. Cheeseman, G. Scalmani, V. Barone, B. Mennucci and G. Petersson, *Inc., Wallingford, CT*, 2009, 200.
28. P. G. Jessop, D. J. Heldebrant, X. Li, C. A. Eckert and C. L. Liotta, *Nature*, 2005, 436, 1102-1102.

Table 1 Main vibration frequency of CO_2, -NH_2, IM, TS and P for Br system optimized at B3LYP/6-311++G(d,p) levels.

Species	Vibrational mode assignment	CO_2+[aEMMIM][Br]	
		Frequency (cm^{-1})	IR intensity
CO_2	ν_s	1327	0
	ν_{as}	2319	711.718
-NH_2	ν_s	3307.84	62.3072
	ν_{as}	3411.419	16.4469
IM	$\nu_s(CO_2)$	1368.18	2.7631
	$\nu_{as}(CO_2)$	2412.17	622.7869
	δ(-NH_2)	1659.76	21.5748
	ν_s(-NH_2)	3418.29	102.9603
	ν_{as}(-NH_2)	3544.87	15.3888
TS	ν_s (-CO_2)	1272.69	327.4269
	ν(C26=O28)	1841.37	549.2495
	ν(-O27-H23)	-1739.73	1966.3709
	ρ(-O27-H23)	1364.12	33.0733
	δ(-O27-H23)	2151.24	7.7407
	ρ(-N22-H_2)	988.33	20.0828
	δ(-N22-H_2)	1464.45	34.8974
	ν(-N22-H24)	3145.71	369.5383
P	ν (C26=O27)	1713.234	397.8789
	ρ(-N22-H24)	740.5431	45.2762
	ρ(-O28-H23)	1198.572	29.7077
	δ(-O28-H23)	1318.498	483.5828
	δ(-N22-H24)	1524.653	327.4707
	ν(-N22-H24)	3163.163	531.7494
	ν(-O28-H23)	3634.93	55.5200

Frequencies scaled by 0.983 for below 1700 $cm^{-1}$and 0.958 for above 1700 cm^{-1}.

401 **Table 2** The electron density (ρBCP), Laplacian of the electron density (∇^2ρBCP) and
402 matrix eigenvalues (λ_1, λ_2, λ_3) for Br system at B3LYP/6-311++G(d,p) level.

	A-B Bond	ρ(r)	$\nabla^2\rho(r)$	ε	λ_1	λ_2	λ_3
	N22-H24	0.33604	-1.461	0.04985	-1.215	-1.157	0.9109
	N22-H23	0.33104	-1.561	0.04282	-1.240	-1.189	0.8671
IM	C26-N22	0.011609	0.03741	0.8435	-0.00977	-0.00530	0.05248
	O28-C26	0.45552	-0.03204	0.00328	-1.191	-1.187	2.345
	O27-C26	0.45838	0.00389	0.00278	-1.199	-1.195	2.398
	N22-H23	0.15688	-0.1870	0.1114	-0.4310	-0.3878	0.6318
	N22-H24	0.31461	-1.536	0.01756	-1.190	-1.169	0.8230
	C26-N22	0.22592	-0.4328	0.02057	-0.4417	-0.4328	0.4417
TS	O27-C26	0.42553	-0.1369	0.09834	-1.132	-1.031	2.027
	O28-H23	0.14791	-0.05183	0.09744	-0.4161	-0.3791	0.7433
	O28-C26	0.35641	-0.6654	0.1146	-0.8797	-0.7893	1.004
	H24-N22	0.32223	-1.595	0.04656	-1.238	-1.183	0.8253
	C26-N22	0.32289	-0.9836	0.1807	-0.7333	-0.6211	0.3709
P	O27-C26	0.41648	-0.3667	0.1089	-1.103	-0.9951	1.732
	O28-H23	0.36243	-2.520	0.01930	-1.790	-1.756	1.025
	O28-C26	0.29651	-0.5787	0.03594	-0.6515	-0.6289	0.7017

403

Table 3 The main donor-acceptor interactions and their second order perturbation stabilization energies, E(2) as well as orbital energy gap for Br system calculated at B3LYP/6-311++G(d,p) level.

	Donor(i)	Acceptor(j)	E(2)/(kJ/mol)	E(j)-E(i)/(a.u.)
	LP(3)O28	BD*(2)C26-O27	509.4	0.32
IM	LP(2)O28	BD*(3)C26-O27	499.8	0.33
	LP(1)O28	BD*(1)C26-O27	62.67	1.47
	LP(1)N22	BD*(1)C26-C19	34.94	0.65
	LP(2)O28	BD*(1)N22-H23	505.6	0.49
TS	LP(3)O28	BD*(2)C26-O27	240.2	0.35
	LP(2)O27	BD*(1)N22-C26	172.3	0.47
	LP(2)O27	BD*(1)N22-C26	91.71	0.72
	LP(2)O28	BD*(1)C26-O27	129.3	0.60
P	LP(1)N22	BD*(1)C26-O28	115.2	0.49
	LP(2)O28	BD*(1)C26-O28	90.79	0.70
	LP(2)O27	BD*(1)C26-O28	70.67	0.54

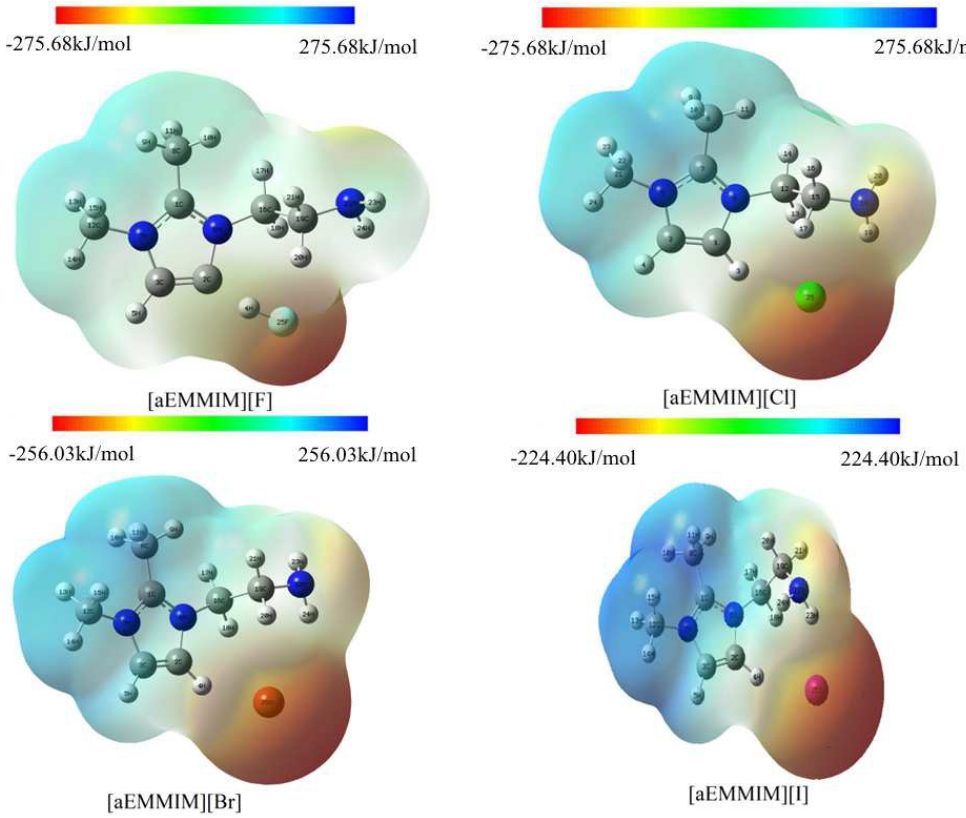

408

409 **Figure 1** 3D plots of the electrostatic potential surface for the pure ILs, including

410 [aEMMIM][F], [aEMMIM][Cl], [aEMMIM][Br], [aEMMIM][I], optimized at

411 B3LYP/6-311++G(d, p) level, respectively.

412

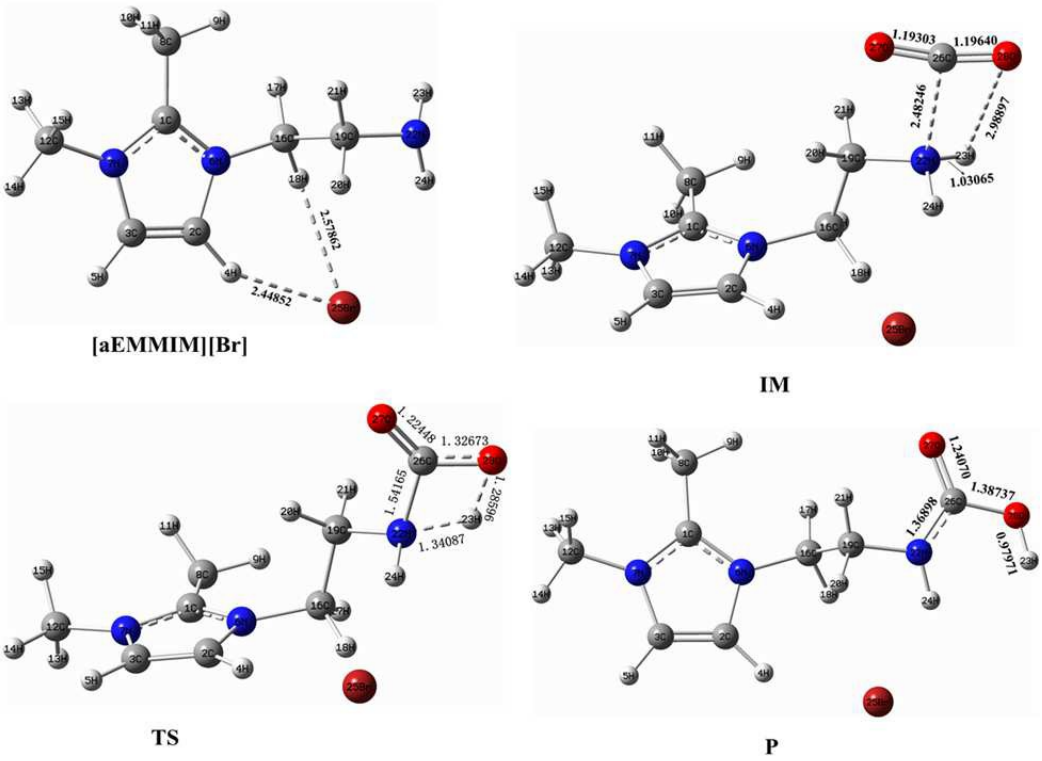

Figure 2 Geometrical parameters of Br system, including [aEMMIM][Br], IM, TS and P, optimized at B3LYP/6-311++G(d, p) level, respectively. (in Å)

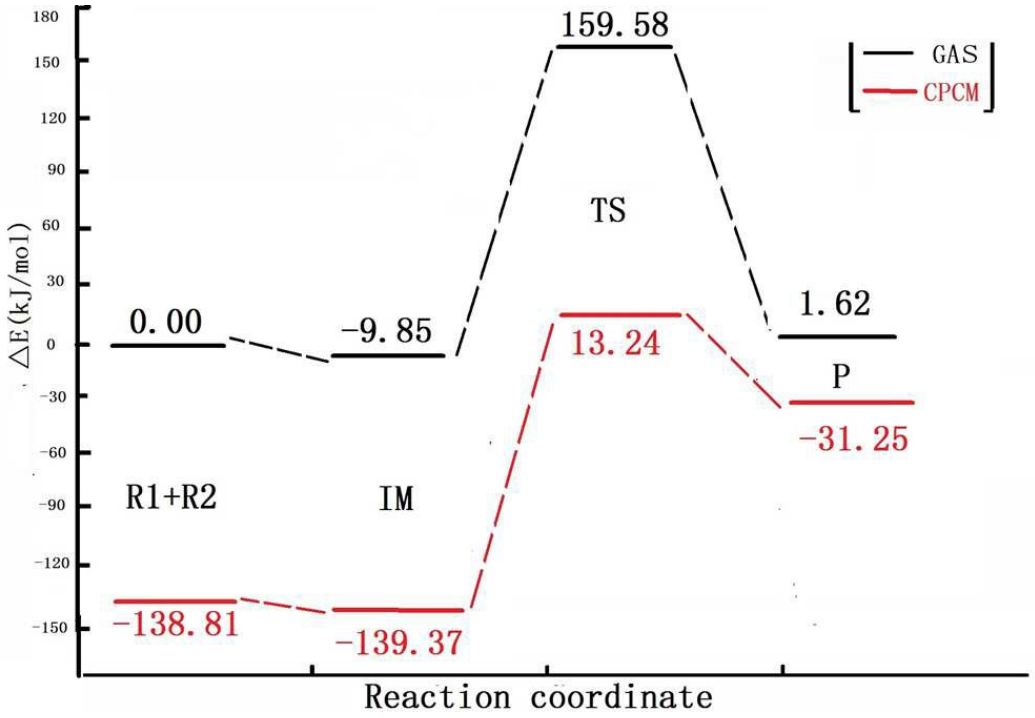

417

418 **Figure 3** Potential energy surface (PES) profile of [aEMMIM][Br] capture CO_2

419 optimized at B3LYP/6-311++G (d, p) level.

420

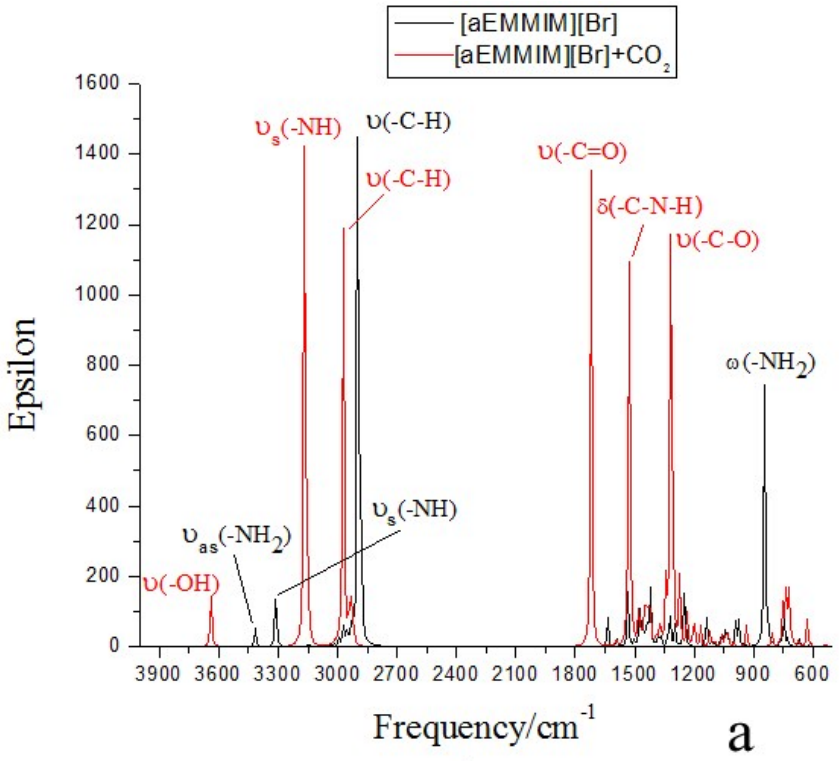

421

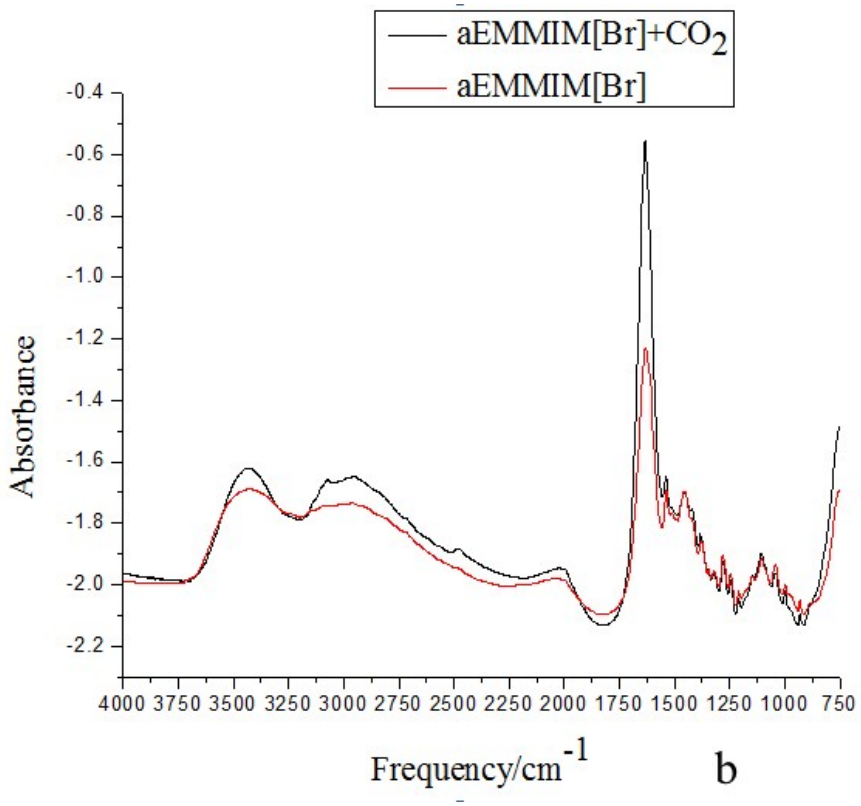

422

423 **Figure 4** Computational IR spectrum (a) and experimental IR spectrum (b) of
424 [aEMMIM][Br] and [aEMMIM][Br]+CO_2.

425

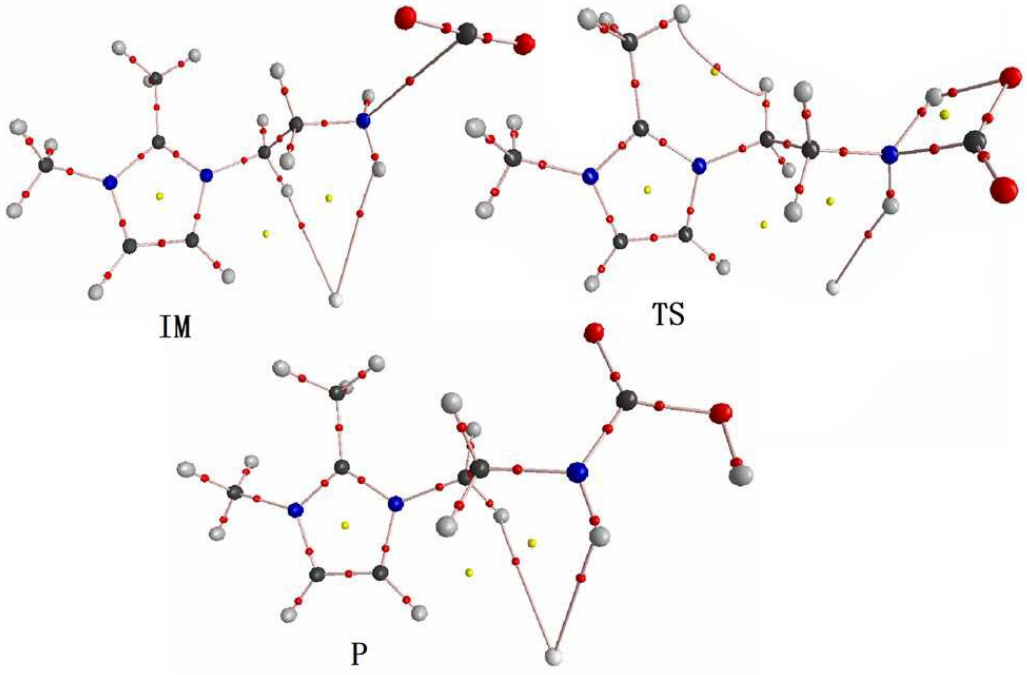

Figure 5 Molecular graph of [aEMMIM][Br] capture CO_2 optimized at B3LYP/6-311++G(d,p) level, red points and yellow points correspond to bond critical point(BCP) and ring critical point(RCP), respectively.

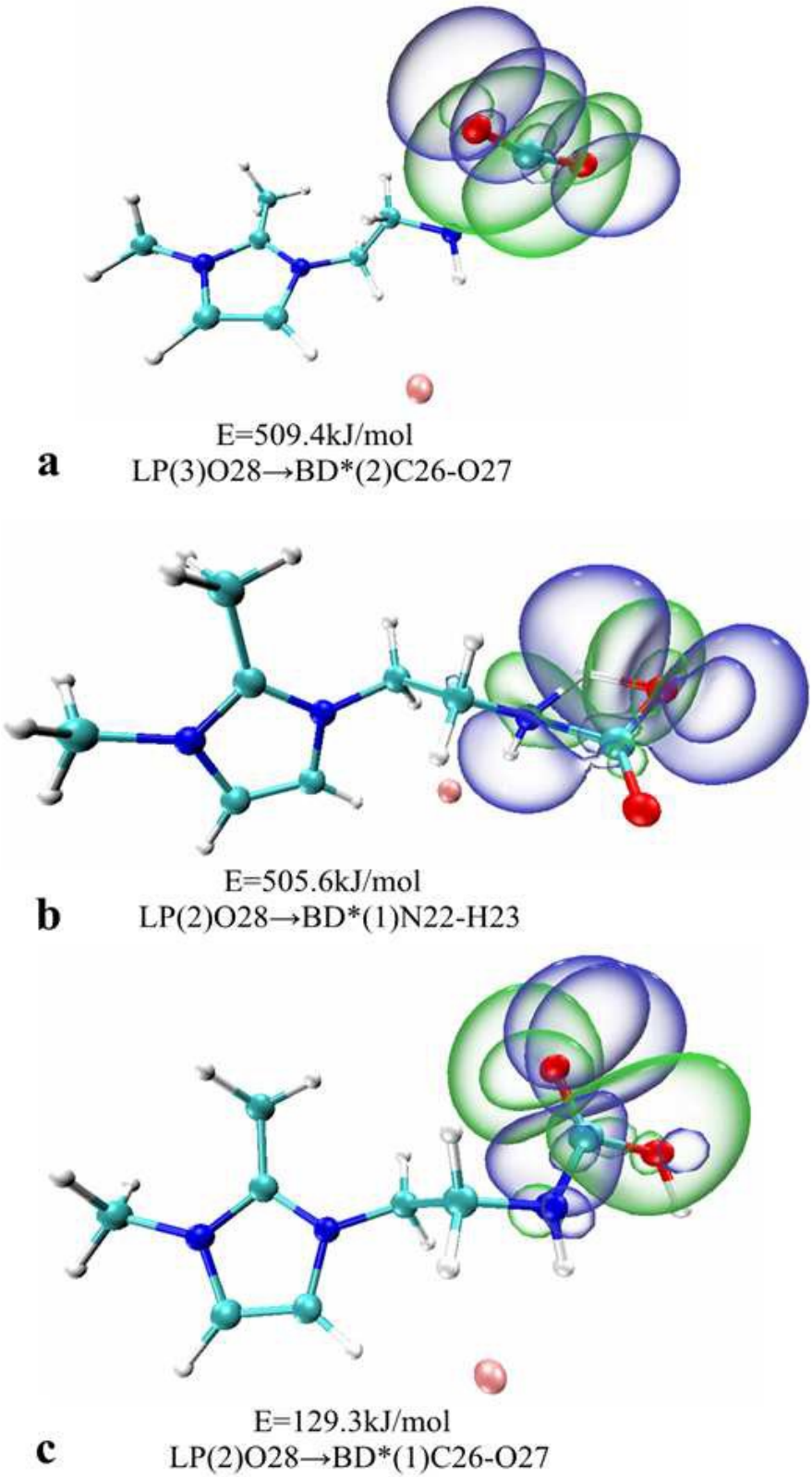

Figure 6 The schematic graphs of electron transfer of Br system based on the NBO analysis (a form IM, b for TS and C for P).

Graphical Abstract

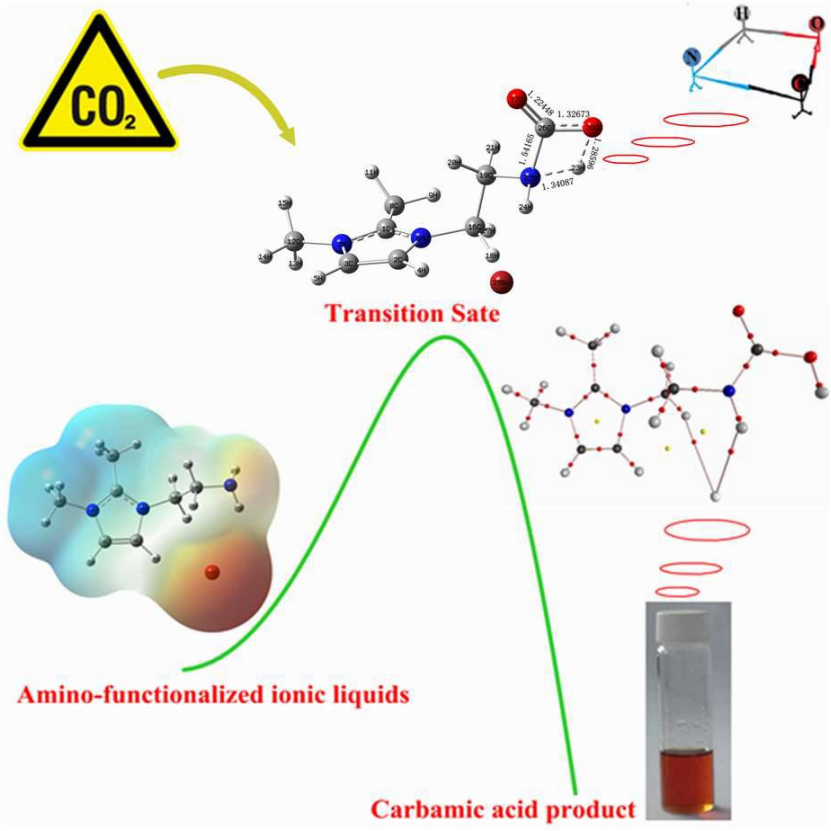

Both computational and experimental studies show amino-functionalized ionic liquids，[aEMMIM][X] (X=F, Cl, Br, I), can chemically capture CO_2.